

# **ACOUSTIC, PIEZOELECTRIC AND OPTOACOUSTIC PROPERTIES OF ORGANIC MATERIALS**

**3rd and FINAL TECHNICAL REPORT  
by  
PROFESSOR JOHN N SHERWOOD**

**SEPTEMBER 1999**

**United States Army**

**EUROPEAN RESEARCH OFFICE OF THE U.S. ARMY**

**London, England**

**CONTRACT NUMBER N68171-98-M-5166**

*R+D no: 8212-CH-01*

**University of Strathclyde, Glasgow, Scotland, UK**

**Approved for Public Release; distribution unlimited**

**20000118 067**

REPORT DOCUMENTATION PAGE

Form Approved  
OMB No. 0704-0188

Public reporting burden for this collection of information is estimated to average 1 hour per response, including the time for reviewing instructions, searching existing data sources gathering and maintaining the data needed, and completing and reviewing the collection of information. Send comments regarding this burden estimate or any other aspect of this collection of information, including suggestions for reducing this burden, to Washington Headquarters Services, Directorate for Information Operations and Reports, 1215 Jefferson Davis Highway, Suite 1204 Arlington, VA 22202-4302, and to the Office of Management and Budget, Paperwork Reduction Project (0704-0188), Washington, DC 20503.

1. AGENCY USE ONLY (Leave Blank) 2. REPORT DATE  
September 1999

3. REPORT TYPE AND DATES COVERED  
3rd and Final Report September 1999

4. TITLE AND SUBTITLE  
ACOUSTIC, PIEZOELECTRIC AND OPTO ACOUSTIC PROPERTIES OF ORGANIC MATERIALS

5. FUNDING NUMBERS  
C-N68171-M-5166

6. AUTHOR(S)  
PROFESSOR JOHN N, SHERWOOD

7. PERFORMING ORGANIZATION NAME(S) AND ADDRESS(ES)  
UNIVERSITY OF STRATHCLYDE  
295 CATHEDRAL STREET  
GLASGOW G1 1XL, SCOTLAND, UK

8. PERFORMING ORGANIZATION REPORT NUMBER  
960513

9. SPONSORING/MONITORING AGENCY NAME(S) AND ADDRESS(ES)  
UAARDSG-UK Fiscal Office  
Edison House  
223 Old Marylebone Road, London NW1 5TH

10. SPONSORING/MONITORING AGENCY REPORT NUMBER

11. SUPPLEMENTARY NOTES

12a. DISTRIBUTION/AVAILABILITY STATEMENT

12b. DISTRIBUTION CODE

13. ABSTRACT (Maximum 200 words)

Studies have been made of the acoustic, piezoelectric and optoacoustic properties of two acentric organic crystals (-2)- $\alpha$ -methyl benzylamino-4-nitropyridine (MBANP) and (-2)- $\alpha$ -methyl benzylamino-3-methyl-4-nitropyridine (3Me-MBANP).

These include

- a) a full study of the linear and non-linear optics of 3Me-MBANP
- b) the piezoelectric coefficient  $d_{23}$  of MBANP
- c) the photoelastic coefficients of MBANP

In all properties the materials show excellent performance and have promise for use as potential device materials.

14. SUBJECT ITEMS  
Refractive indices, Sellmeier equations, linear optics, piezoelectric effect, opto-acoustic effect, linear electro-optic effect.

15. NUMBER OF PAGES  
27

16. PRICE CODE

17. SECURITY CLASSIFICATION OF REPORT  
UNCLASSIFIED

18. SECURITY CLASSIFICATION OF THIS PAGE  
UNCLASSIFIED

19. SECURITY CLASSIFICATION OF ABSTRACT  
UNCLASSIFIED

20. LIMITATION OF ABSTRACT  
SAR

# CONTENTS

	<u>Page</u>
1. INTRODUCTION	1
BACKGROUND	1
PERSONNEL	2
2. MATERIALS	3
MATERIAL CHARACTERISTICS	3
<i>MBANP</i>	3
<i>3 Me-MBANP</i>	4
CRYSTAL GROWTH	4
<i>Growth from Solution</i>	4
<i>Growth from the Melt</i>	5
CRYSTAL PERFECTION	5
3. LINEAR AND NON-LINEAR OPTICS OF 3-METHYL-MBANP	7
SAMPLE PREPARATION	7
<i>Preparation of Prisms from the Bridgman Grown Crystal</i>	7
<i>Preparation of Prisms from the Solution Grown Crystal</i>	8
EVALUATION OF REFRACTIVE INDICES	8
SPECTROSCOPY	12
PHASE MATCHING LOCUS AND CRITICALITY CURVES	14
4. MEASUREMENT OF THE PIEZOELECTRIC COEFFICIENTS OF MBANP BY AN INTER- FEROMETRIC METHOD	17
EXPERIMENTAL PROCEDURE	17
RESULTS AND DISCUSSION	19

<b>5.</b>	<b>MEASUREMENT OF ACOUSTO-OPTIC COEFFICIENTS OF MBANP</b>	<b>21</b>
	THEORY	21
	EXPERIMENTAL EQUIPMENT	22
	EXPERIMENTAL PROCEDURE AND RESULTS	24
<b>6.</b>	<b>SUMMARY AND FUTURE WORK</b>	<b>27</b>

# 1. INTRODUCTION

## BACKGROUND

The original proposal which led to this award defined a three year programme which envisaged the evaluation of the non-linear optical, piezoelectric and opto-acoustic properties of non-centrosymmetric, highly polar organic materials. The proposal allowed for the purchase of equipment for the evaluation of these properties to supplement that already available. The supplementary equipment was particularly required for the evaluation of the acousto-optic properties. The proposal also provided for personnel to carry out the programme.

In the event, support was only available for a 12-month proving study which provided support for personnel (one postdoctoral research worker) together with some ancillary support for consumable items.

Using this support, an evaluation was made of the feasibility of the programme using existing equipment.

This report summarises the results of that feasibility study and details sequentially

- materials preparation and evaluation
- non-linear optical assessment
- piezoelectric assessment
- opto-acoustic assessment

## PERSONNEL

This wide range of studies was achieved in 12 months through the efforts of a number of colleagues who were supported by the grant

Dr P. Kerkoc<sup>1</sup> (six months), Dr P. Datta<sup>2</sup> (six months) and Dr D. Hayward (two months) - piezoelectric and acoustic measurements

from ancillary funds provided by the UK EPSRC

Dr S. Lochran<sup>3</sup> - optical measurements

and by contributions from visiting scientists

Professor K. Siomos<sup>4</sup>

The support of my colleague, Dr F.R. Cruickshank, in the supervision of the programme is also gratefully acknowledged.

Current addresses:

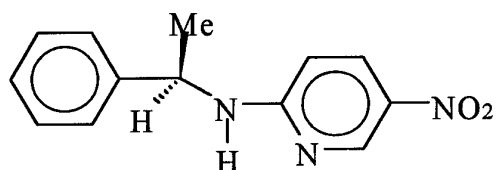
1. Centre of University Studies of Koper, Cankarjeva 5, 6000 Koper, Slovenia
2. Laser Physics Group, Physical Research Lab., Navrangpura, Ahmedabad 380 009, India
3. GEC Marconi Avionics Ltd, Radar Systems Division, Ferry Road, Edinburgh EH5 2XS
4. Department of Biophysics, University of Athens, Greece

## 2. MATERIALS

### MATERIAL CHARACTERISTICS

Two related materials were chosen for examination both of which were shown to have strong non-linear optical properties. The molecular and structural properties of these are summarised below.

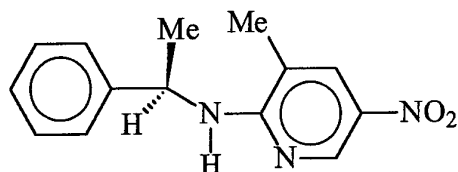
(-)-2- $\alpha$ -methyl benzylamino-4-nitropyridine (MBANP)



Crystallographic characteristics [1]

Monoclinic, space group  $P2_1$  with  $a = 0.5392\text{nm}$ ,  $b = 0.6354\text{nm}$ ,  $c = 1.7924\text{nm}$ ,  $\beta = 94.6^\circ$  and  $z = 2$ .

(-)-2- $\alpha$ -Methyl benzylamino-3-methyl-4-nitropyridine (3Me - MBANP)



Crystallographic characteristics [2]

Orthorhombic, space group  $P2_12_12_1$  with  $a = 0.5481\text{nm}$ ,  $b = 0.6791\text{nm}$ ,  $c = 3.5877\text{nm}$ ,  $\beta = 90^\circ$  and  $z = 4$ .

### **MBANP**

This material which has been widely studied by this group [3] was chosen because of our general familiarity with its properties. Study of its crystal growth behaviour [4] has led to the production of samples of high perfection in sizes up to  $10 \times 5 \times 5 \text{cm}^3$  (Figure 1). It can be readily cut and shaped into samples of sufficient size and suitable orientation for the proposed measurements and polished to optical standards. The quality of the material is well defined by Figure 2.1.

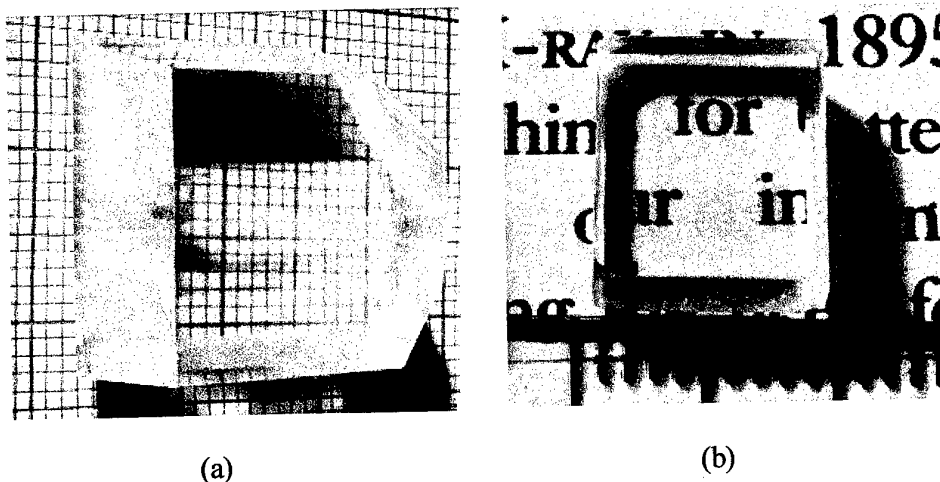


Figure 2. 1(a) Crystal of MBANP grown from saturated methanol solution by the temperature lowering technique, (b) A cut and polished optical blank of MBANP.

### **3Me-MBANP**

Many organic materials are difficult to cut and polish due to their softness and tendency to cleave. This material was designed and synthesised [5] to counteract these tendencies. Due to the difference in crystallographic structure 3Me-MBANP shows a much higher surface hardness than MBANP. This contributes much to the greater ease of polishing of the samples than for the softer MBANP. Prior to the commencement of this programme this material had only been subjected to a preliminary evaluation.

## **CRYSTAL GROWTH**

Purification of 3Me-MBANP by column chromatography (silica gel and alumina with dichloromethane [6]) and zone refining yielded material of 99.99% purity (vapour phase chromatography)

### **Growth from Solution**

The material showed satisfactory solubility in a range of solvents but yielded the best quality plate-like crystals from solution in acetone (solubility 1g/30ml at 25°C). Seeded growth from this solution in a crystalliser using the temperature lowering technique [7] at a rate of 0.05°/day gave tablet-like crystals of good quality. Successive growth attempts using seeds of selected orientation [4] yielded high quality prismatic specimens in sizes up to 40x30x30mm<sup>3</sup> all of good visual quality (Figure 2.2a).

### ***Growth from the Melt***

Growth from the melt in a standard Bridgman system using a double jacketed tube [7] and temperature gradient  $\sim 7^\circ/\text{cm}$  yielded good quality specimens 1cm diameter x 10 cm long. There were not single crystals but contained volumes of single crystal of a size large enough to allow the preparation of operational specimens  $2 \times 2 \times 0.5 \text{ cm}^3$  (Figure 2.2b).

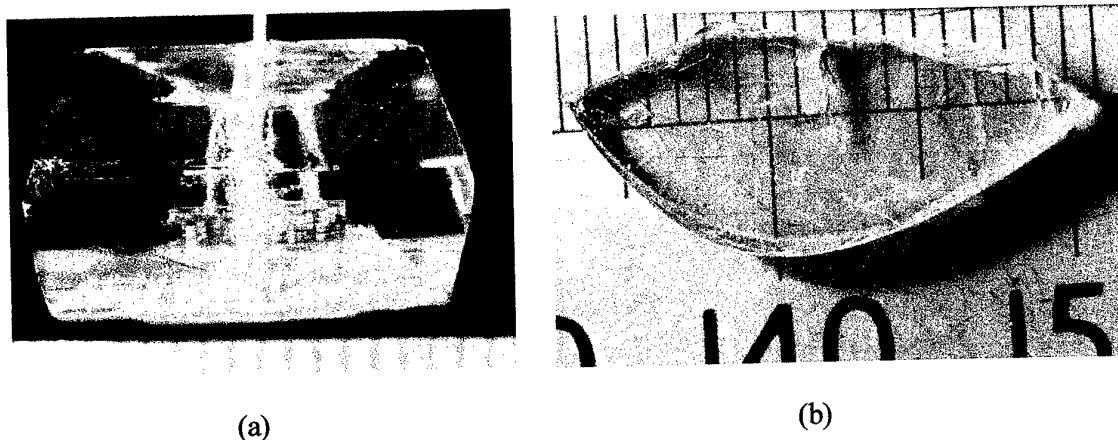


*Figure 2.2 Crystals of 3Me-MBANP grown from (a) solution in acetone (b) the melt by the Bridgman technique*

### **CRYSTAL PERFECTION**

X-ray section topography [8] revealed the crystals grown from solution to be of high structural perfection containing relatively large volumes of low dislocation content (Figure 2.3). Crystals grown from the melt showed the higher dislocation content which has come to be expected of crystals grown under the constraints of a closed ampoule. Despite this, the crystals were still of high optical clarity.

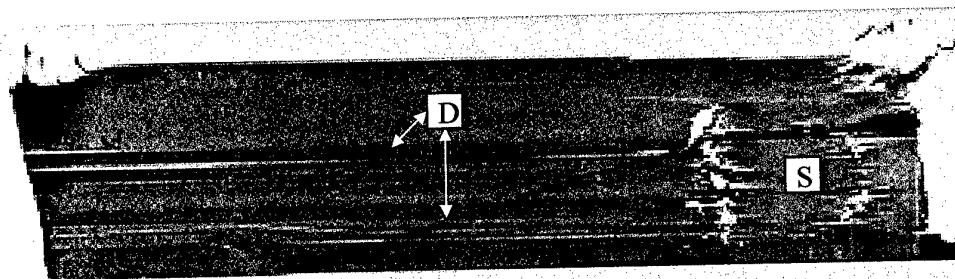


*Figure 2.3. X-ray section topograph of a (001) section of a crystal of 3Me-MBANP grown from solution in acetone. The few ( $\sim 4$ ) dislocations (D) spread only from the seed (S) on the right of the left facet. Otherwise the crystal is perfect.*

## REFERENCES

1. R.J. Tweig and C.W. Dirk, Res. Report RJ5237 (54077) IBM Almaden Research Centre, San Jose, California, 1986.
2. R.J. Tweig, A. Azema, K. Jain and Y.Y. Cheng, Chemical Physics Letters, 1982, 92, 208.
3. R.T. Bailey, F.R. Cruickshank, S.M.G. Guthrie, B.J. McArdle, H. Morrison, D. Pugh, E.E.A. Shepherd, J.N. Sherwood and C.S. Yoon, R. Kashyap, B.K. Nayar and K.I. White, J. Modern Optics, 1988, 35, 511.
4. P.J. Halfpenny, H. Morrison, R.I. Ristic, E.E.A. Shepherd, J.N. Sherwood, G.S. Simpson, C.S. Yoon, Proc. Roy. Soc., 1993, A440, 683.
5. Synthesis adapted from G.F. Hawkins and A. Roe, J. Organic Chemistry, 1949, 14, 328.
6. P.J. Halfpenny, J.N. Sherwood and G.S. Simpson, Proc. International School of Physics "Enrico Fermi", Course 126, Non-linear Optical Materials: Principles and Applications, IOS Press, Amsterdam. 1995 p131.
7. B.J. McArdle and J.N. Sherwood, Advanced Crystal Growth, Edited by P.M. Dryburgh, B. Cockayne and K.G. Barraclough, Prentice Hall, New York .1987. p 179.
8. B.K. Tanner, X-Ray Diffraction Topography, Pergamon, Oxford. 1976.

### 3. LINEAR AND NON-LINEAR OPTICS OF 3-METHYL-MBANP

Basic to the understanding and interpretation of the piezoelectric and acousto-optic studies is a knowledge of the linear optics of the two materials. As noted above, previous studies of MBANP have led to a full optical characterisation of this material. Up to the present time no such characterisation has been made of 3-Me MBANP. This section details the results of a study of these properties.

#### SAMPLE PREPARATION

##### *Preparation of Prisms from the Bridgman Grown Crystal*

3-methyl-MBANP possesses a natural (001) cleavage plane, which was used to facilitate the orientation and preparation of the first prism. The faces used as the input and output faces were the (100) and a face at an angle to this respectively. This was achieved by cutting and polishing the (100) to optical quality and mounting the sample on a perspex counter prism with the (100) face flat. This combination was placed on the polishing jig and the sample lapped and polished. This produced a prism with an input and output face at an angle equal to the counter prism angle and with the Z dielectric axis as the prism axis.

##### *Preparation of Prisms from the Solution Grown Crystal*

The second prism to be used in the refractive index determination was cut from a solution grown crystal. This was done to check the reproducibility of the refractive indices between both crystal types and because the orientation of prisms is easier with solution grown crystals owing to the increased number of naturally defined faces. The orientation of the prism with respect to the crystal morphology is shown below (Fig. 3.1)

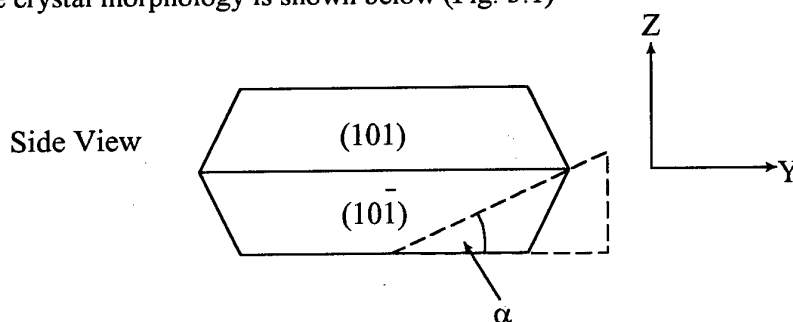


Fig.3.1 Orientation of 3-methyl-MBANP solution grown crystal with respect to crystal morphology. The prism axis is parallel to the X dielectric axis.

When polished in the same manner as the Bridgman crystal, a prism is produced which has the (001) cleavage plane as its input face.

In both cases the time taken to lap and polish these materials to optical flatness was considerably lower (1 hour) than usually experienced with this class of material. This reflects the increased surface hardness compared with that for other organic solids, e.g. MBANP.

## EVALUATION OF REFRACTIVE INDICES

The first step in the evaluation of the refractive indices is the measurement of the prism apex angle,  $\alpha$ , which is defined by the angle of the counter prism. Each prism was mounted on the rotatable stage of a spectroscope. Several pieces of information can be gained by reflecting a He/Ne laser from the faces of the prisms. Firstly, the apex angle can be measured by the back reflection technique and the angles are given in Table 2.1 for both prism types. Secondly, the parallelism of the faces can be measured by the same back reflection technique, but by observing the difference in height of the reflected spots. By this technique the faces were found to be parallel to within  $0.2^\circ$ . Thirdly, from the quality of the transmitted laser beam, an indication of the optical quality of the polished faces and of the bulk crystal can be obtained. It should be noted that, despite the short polishing time, the integrity of the laser spot was excellent and was preserved with minimal scattering.

Prism Type	$\alpha$ / degrees
Bridgman	$16.700 \pm 0.008$
Solution	$13.467 \pm 0.008$

Table 3.1. 3-methyl-MBANP prism apex angles.

With the prism apex angle known, the refractive indices can be measured using the minimum deviation technique. For the Bridgman grown crystal, the prism axis was parallel to the Z dielectric axis giving the principal Z refractive index using the minimum deviation technique directly. The refractive index in the Y direction was obtained from the orthogonal polarisation using a composite refractive index technique<sup>2</sup>. A typical curve is shown in Fig. 3.2 where the error bars represent an error of  $\pm 0.005$ .

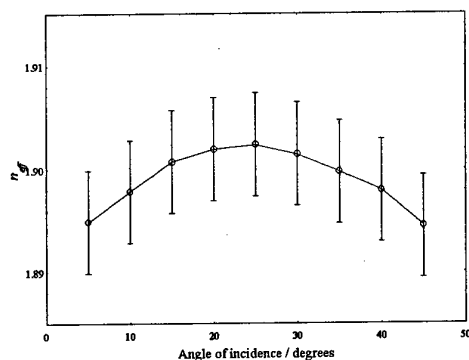


Fig. 3.2. Variation of  $n_{eff}$  with angle of incidence for a Bridgman grown crystal at  $\lambda = 530$  nm.

The dispersion of both refractive indices is given in Fig. 3.3 where the error bars represent an error of  $\pm 0.005$ .

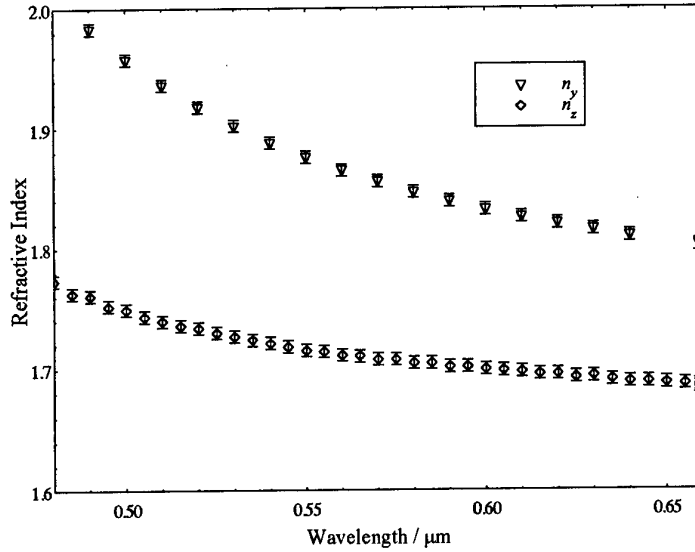


Fig. 3.3. Refractive index dispersion curves for a Bridgman grown crystal.

For the solution grown crystal, the prism axis was parallel to the X dielectric axis which gave the principal X refractive index from the minimum deviation technique and the principal Y refractive index from the orthogonal polarisation. The dispersion of these indices is given in Fig. 3.4.

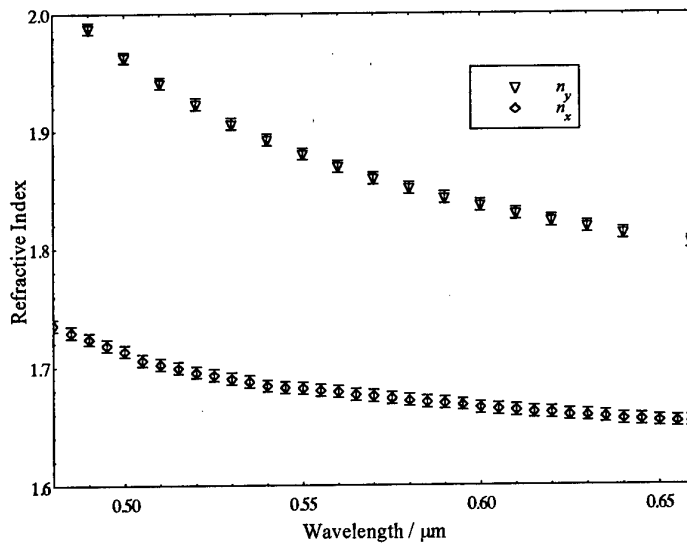


Fig. 3.4. Refractive index dispersion curves for a solution grown crystal.

The Sellmeier equation was fitted to the X and Z refractive indices as shown in Fig. 3.5 and in Fig. 3.6 for the Y refractive indices from both types of prism.

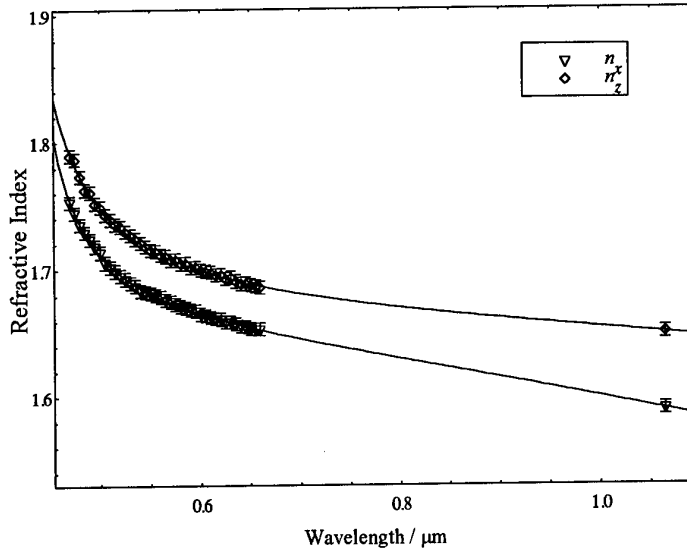


Fig. 3.5. Sellmeier fit to X and Z refractive indices.

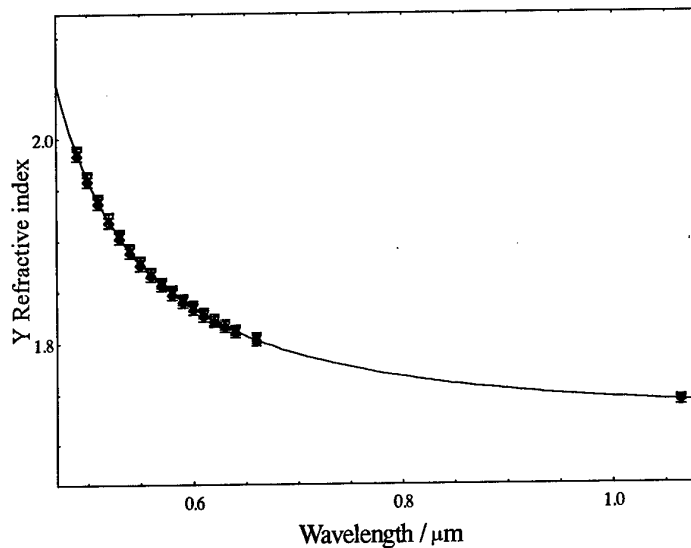


Fig. 3.6. Sellmeier fit to Y refractive indices obtained from Bridgman and solution grown crystals.

The refractive indices in the Y direction obtained from the two types of prism agreed with each other within the experimental error of  $\pm 0.005$ . This increases the confidence in the measurements of  $n_y$ , since the data were obtained independently and from different crystals and also confirms the accuracy with which the crystals were cut and polished in both cases.

The data points at  $1.064\mu\text{m}$  were obtained by comparison of the experimentally determined phase matching angles with theoretically determined positions. The refractive indices at  $1.064\mu\text{m}$  were adjusted until the phase matching angle agreed with the experimentally determined position. This procedure is very sensitive to variations in refractive index and the new values obtained are accurate to within  $\pm 0.005$ . The quality of this agreement is shown in Table 3.2.

Orientation	Experimental Position / deg	Theoretical Position / deg
(101)	31.5	32.2
(110)	49	38.01
(011)	19.4	17.1

Table 3.2. Theoretical and experimental phase matched peak agreement.

The Sellmeier parameters for all refractive indices are given in Table 3.3.

Index	A	B	C	D	max. dev.
$n_x$	2.67839	0.0919939	0.175789	0.230901	0.00208
$n_y$	2.35431	0.581332	0.152215	0.00922734	0.00288
$n_z$	2.63522	0.153796	0.163522	0.0811653	0.00506

Table 3.3. Sellmeier parameters for 3-methyl-MBANP, valid in the range from 470nm to 1064nm.

The order of the refractive indices places the phase matching of 3-methyl-MBANP in Hobden<sup>1</sup> class eight.

The relatively high values of the refractive index in the Y direction can be explained on the basis of the orientation of the molecules in the unit cell. The molecular arrangement in the YZ plane is shown in Fig. 3.7.

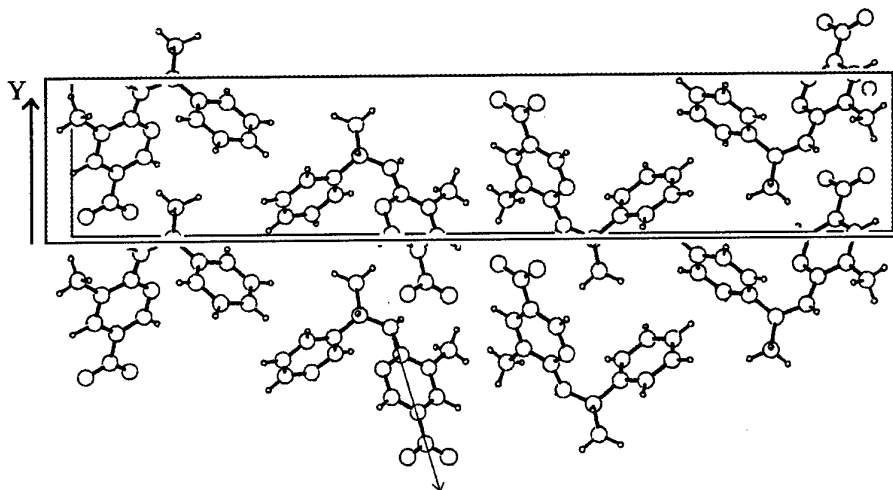


Fig. 3.7. Molecular orientation in the principal YZ dielectric plane.

As can be seen from Fig. 3.7, the charge transfer axis, depicted by the arrow superimposed on the lower molecule, lies from the nitrogen atom of the nitro amino group to the nitrogen atom of the nitro group. This axis is the most polarisable axis of the molecule and makes an angle of  $30.8^\circ$  to the Y dielectric axis as calculated from X-ray data. It is therefore expected that the Y direction would have the largest refractive index. The refractive indices in the other directions will then be much smaller than that in the Y direction by virtue of the fact that the charge transfer axis lies at increased angles of  $66.1^\circ$  to the X dielectric axis and  $71.8^\circ$  to the Z

dielectric axis. Due to the relatively arbitrary definition of the direction of the charge transfer axis and the small difference between the X and Z refractive indices, no conclusions can be made concerning the correlation between the relative magnitudes of the indices in the X and Z directions and the angles to the charge transfer axis other than that they should be similar and lower than the Y value.

### SPECTROSCOPY OF 3-METHYL-MBANP

The square root of the Sellmeier  $C$  parameter gives an indication of the UV / visible absorption band centre of the molecule. The wavelength of the onset of optical absorption in a crystal is known as the absorption edge and the edge occurs at different wavelengths depending the polarisation vector. It is expected that the absorption of the Y polarisation would occur at the longest wavelength since the most polarisable axis of the molecule lies closest to the Y direction.

The spectrum of 3-methyl-MBANP was determined using a Perkin-Elmer UV / Visible Spectrophotometer Model 402. A polariser was placed in the sample arm of the instrument in order to select the polarisation of the incident light. Three optically polished samples of the bulk material with their input faces parallel to the (101), (110) and (001) crystallographic planes respectively, were prepared for this characterisation. The onset of absorption (absorption edge), which is defined as the point at which the optical density has changed by 0.1, for light polarised in each direction is given in Table 3.4.

Direction	Edge / nm	$\sqrt{C}$ / nm
X	465	429
Y	500	390
Z	480	404

Table 3.4. Positions of absorption edges and band centre predictions.

It should be noted that the error in determining the optical density is  $\pm 0.05$  owing to fluctuations in the baseline.

The refractive indices of 3-methyl-MBANP are in the order of  $n_y > n_z > n_x$  and, as can be seen from Table 4, the onset of absorption for light polarised in the Y direction, occurs at the longest wavelength and at the shortest wavelength for light polarised in the X direction. This is consistent with the simple model which predicts that the direction of largest refractive index possesses an absorption edge at the longest wavelength. This model assumes that the refractive indices for each direction are equal at very long wavelengths. Therefore, as the wavelength is decreased, it can be seen that the direction with the largest refractive index will approach a transition before the directions with smaller refractive indices and hence the absorption edge will appear at longer wavelengths for this direction. Although the results obtained are consistent with the simple model outlined above, they must be treated with caution. The Sellmeier function is a four parameter fit and, as such, the parameters obtained from such a fit are highly dependent on the starting points given. Therefore, the prediction of the positions of the band centres using the square root of the Sellmeier  $C$  parameter must be regarded as indicative rather than seriously valid.

The spectrum of a solution of 3-methyl-MBANP in acetone was also obtained. This was carried out using the same apparatus as before and calibrated using acetone as solvent in both sample and reference cells. With a  $4 \times 10^{-6}$  molar solution of 3-methyl-MBANP in acetone, the spectrum recorded is shown in Fig. 3.8 with a maximum absorbance between 365nm and 370nm.

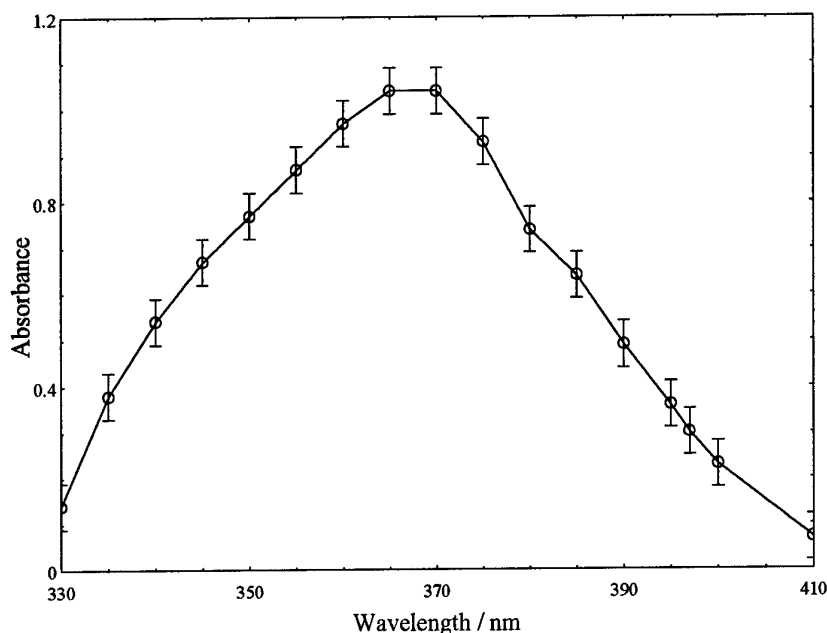


Fig. 3.8. Solution spectrum of 3-methyl-MBANP dissolved in acetone.

At a wavelength of 365nm the absorbance has a value of 1.04, and with a path length of 1cm, the extinction coefficient for 3-methyl-MBANP dissolved in acetone is calculated to be

$$\epsilon = 2 \times 10^5 \text{ M}^{-1} \text{ cm}^{-1}$$

The fact that the solution spectrum absorption edge occurs at a lower wavelength, or higher frequency, than the solid state absorption edge may be due to the lowering of the transition energy by intermolecular interactions in the solid state. Zyss<sup>2</sup> has reported that the position of the absorption edge in the solid state is a result of intermolecular and intramolecular interactions and therefore cannot be determined accurately in the liquid state.

In order to determine the effect of the choice of solvent on the solution spectrum, a solution of 3-methyl-MBANP in cyclohexane was studied in the same manner. The spectrum obtained when the resulting solution was analysed is shown in Fig. 3.9.

As can be seen from the following figure, the peak of absorption occurs at a wavelength of 350nm which is at a shorter wavelength than that of the solution in acetone. This relatively small displacement suggests that the molecule is effectively isolated in both solvents

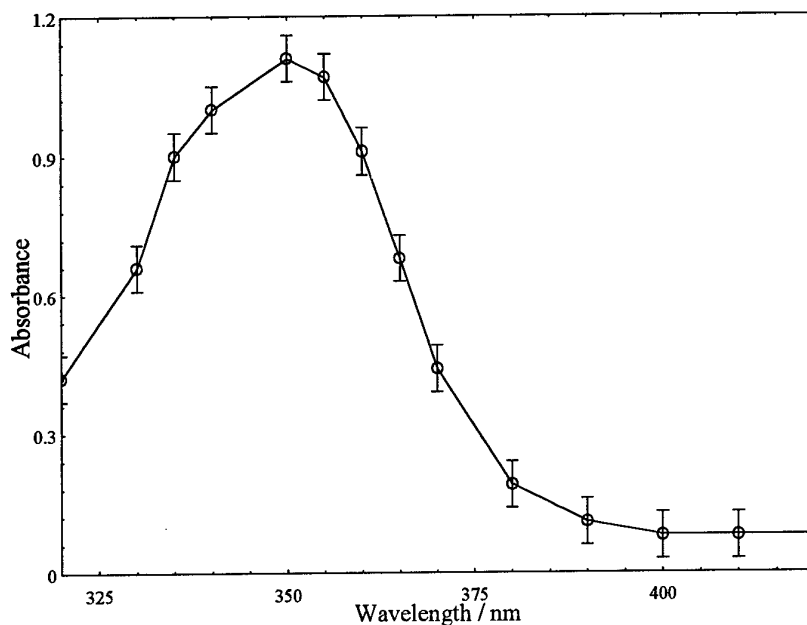


Fig. 3.9. Solution spectrum of 3-methyl-MBANP dissolved in cyclohexane.

### PHASE MATCHING LOCUS AND CRITICALITY CURVES

The phase matching locus at any particular wavelength can be obtained if the principal refractive indices are known. With the principal refractive indices of 3-methyl-MBANP evaluated, the phase matching locus may now be computed. The stereographic projection of the locus is shown in Fig. 3.10 for a fundamental wavelength of 1064nm with the refractive indices used in the calculations given in Table 3.5.

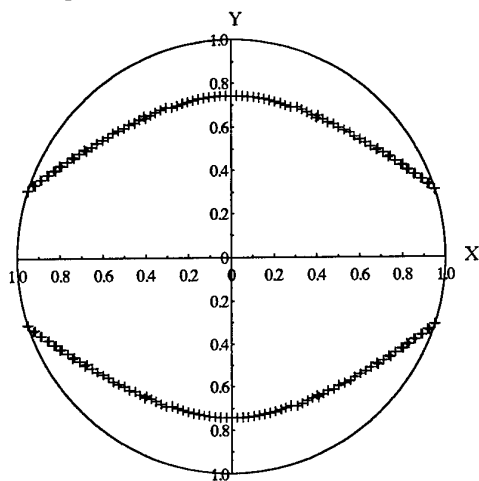


Fig. 3.10. Phase matching locus for 3-methyl-MBANP at a fundamental wavelength of 1064nm. Only Type I phase matching is possible.

Refractive index	1064nm	532nm
$n_x$	1.5893	1.6896
$n_y$	1.7425	1.9014
$n_z$	1.6505	1.7254

Table 3.5. Refractive indices used in the phase matching locus calculation.

The phase matching locus of 3-methyl-MBANP was calculated at a variety of fundamental wavelengths in the same manner as above. A plot of wavelength versus the position in which the phase matched locus intersects a principal dielectric plane is known as a criticality curve. The criticality curve of 3-methyl-MBANP is shown in Fig. 3.11.

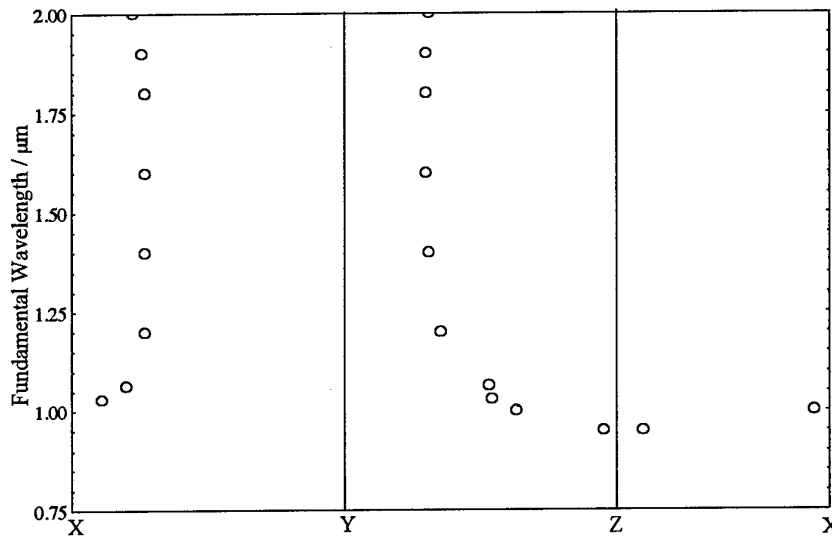


Fig. 3.11. Criticality curves of 3-methyl-MBANP.

There are two very interesting features of this figure which show that this material has potentially very useful applications. Firstly, the rather vertical nature of part of the curve shows that this material can be phase matched at the same internal angle over a wide range of wavelengths. This would allow the frequency doubling of a tunable infrared laser source, such as an optical parametric oscillator or an IR dye laser, with minimal alteration of the phase matching angle of the doubling crystal. The crystal would also be useful in silica fibre based optical communications systems where, due to non-linear effects in the fibre, new frequencies of light are developed in the region of the 1.3 $\mu\text{m}$  minimum loss window. Phase matching of this signal would be possible since the direction of phase matching changes very little with frequency in this region and hence the new frequencies could be accommodated.

There also exists a portion of this curve in which, for a specific, narrow band wavelength range, phase matching is possible over a wide range of angles. When this portion of the curve intersects a dielectric axis, the situation is then known as non-critical phase matching. This has two very important consequences. Firstly, when a material is non-critically phase matched, there exists no walk-off between the bound polarisation wave and the free second harmonic wave. This has the effect of increasing conversion efficiency. Secondly, the propagation direction needed for this condition is the Z dielectric axis which is orthogonal to the natural cleavage plane of 3-methyl-MBANP. This has the advantage that very high

quality optical specimens can be obtained for this purpose by direct cleavage with no need for optical polishing.

#### 4. MEASUREMENT OF THE PIEZOELECTRIC COEFFICIENTS OF MBANP BY AN INTERFEROMETRIC METHOD

In the present experiment, the converse piezoelectric effect is used for the measurement of the coefficients of MBANP. Monoclinic MBANP with diad axis along the Y – dielectric axis has the following piezoelectric tensor.

$$\begin{pmatrix} 0 & 0 & 0 & d_{14} & 0 & d_{16} \\ d_{21} & d_{22} & d_{23} & 0 & d_{25} & 0 \\ 0 & 0 & 0 & d_{34} & 0 & d_{36} \end{pmatrix}$$

The component  $d_{23}$  was measured.

#### EXPERIMENTAL PROCEDURE

An MBANP crystal, accurately cut and polished parallel to about 30 seconds of arc and flat to  $\lambda/10$  is placed in one path of the Mach-Zehnder interferometer. Aluminium mirrors were vacuum deposited on opposite faces of the crystal. A reference phase-plate is placed on the other arm of the interferometer (Fig. 4.1). The optical beam does not transmit through the crystal, but experiences two reflections from the parallel, mirror-coated surfaces of the crystal. On application of a high voltage along an appropriate direction, a strain is generated along the direction of the optical beam. The optical beam experiences a change in path length. This change in path length is manifested at a fixed point in either the change in fringe intensity or a shift of fringe order depending on the magnitude of the strain incurred. By measuring this change of optical path as a function of voltage, one can determine the piezoelectric coefficient.

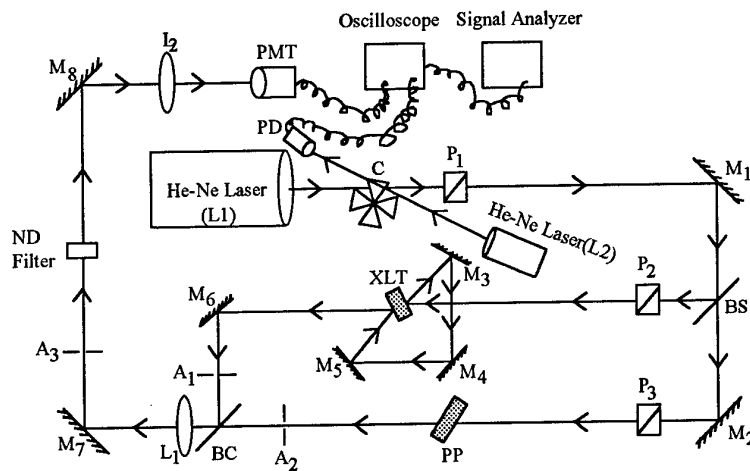


Figure 4.1 Schematic diagram of the Mach-Zehnder Interferometer.

A schematic diagram of the experimental equipment is shown in Fig. 4.8. A He-Ne laser ( $L_1$ ) beam passes through a chopper (C) and polarizer  $P_1$  before being reflected from mirror  $M_1$ . Beam-splitter BS splits the beam into two which serve as the two arms of the Mach-Zehnder interferometer. The MBANP crystal (XTL) is placed in one path and the reference phase-plate (PP) is placed in the other arm. Three mirrors  $M_3$ ,  $M_4$  &  $M_5$  are used to allow the beam to be reflected from the two parallel (mirror coated) surfaces of the crystal. Two further polarisers  $P_2$  and  $P_3$  are placed in the sample and reference path respectively. The sample and reference beams combine at BC after being passed through apertures  $A_1$  and  $A_2$  respectively. The fringes are observed in the image plane of lens  $L_1$ . Another aperture  $A_3$  is used to spatially filter the fringe. The fringe intensity is measured by a photomultiplier (EMI 9558B) operated at 1.5kV.

The crystal samples were cut from a large single crystal. Separate samples of the defined orientation were used for measurement of each coefficient. Mirror coatings are deposited on the polished surfaces. The parallel surfaces along which electric field to be applied need also to be polished for metal electrode deposition. For measurement of  $d_{21}$ , the electrodes are deposited in the (010) faces and the mirror coatings are deposited in the (100) faces. For  $d_{22}$ , the reflector coating as well as electrode coatings are deposited in the (010) faces. Whereas for  $d_{23}$ , the electrodes are in (010) faces and the mirror coatings are in (001) faces. A schematic diagram of the samples are shown in Fig. 4.2.

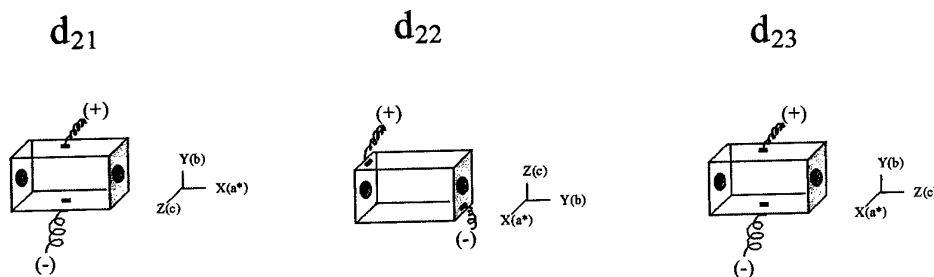


Figure 4.2 Sample orientation and preparation of faces for converse piezoelectric measurements

Measurements are taken in two steps. In the first step, the chopper (C) is switched on and the high voltage is switched off. The chopper signal obtained from photodiode (PD) is used as trigger signal for the oscilloscope and signal analyzer. The phase-plate (PP) is rotated by two vernier divisions and the corresponding PMT signal is noted from the signal analyzer. This measurement is continued until a complete fringe is covered. When this measurement is complete, the phase-plate (PP) is adjusted to a position where the PMT signal is half way between maximum and minimum. This is required to approximately linearise, and maximise the rate of change of, the variation of fringe intensity with phase for the second step of the measurement.

In the second step, the chopper is switched off and it is placed so that the beam from  $L_1$  is passed through whereas the beam from  $L_2$  is blocked. Then the high voltage is switched on. For every high voltage pulse, the peak PMT signal integrated over a large number of pulses is recorded. The voltage pulse as well as PMT signal pulse are recorded as waveforms on a floppy disk and analyzed in a PC with Microcal Origin software.

## RESULTS AND DISCUSSION

The PMT signal vs. phase-plate rotation is plotted in Fig. 4.3. The change in fringe intensity for a given change in path difference is obtained from the linear part of Fig. 4.3. PMT signal pulses corresponding to different voltage pulses are plotted in Fig. 4.4. The change in signal intensities in these curves are transformed into the path difference by using the result of Fig. 4.3 ?.

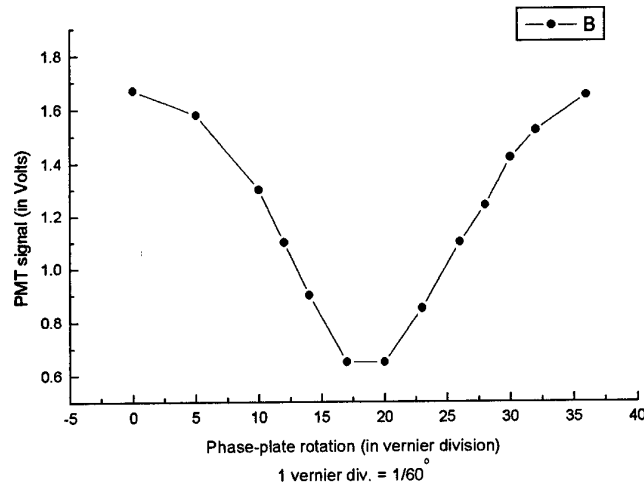
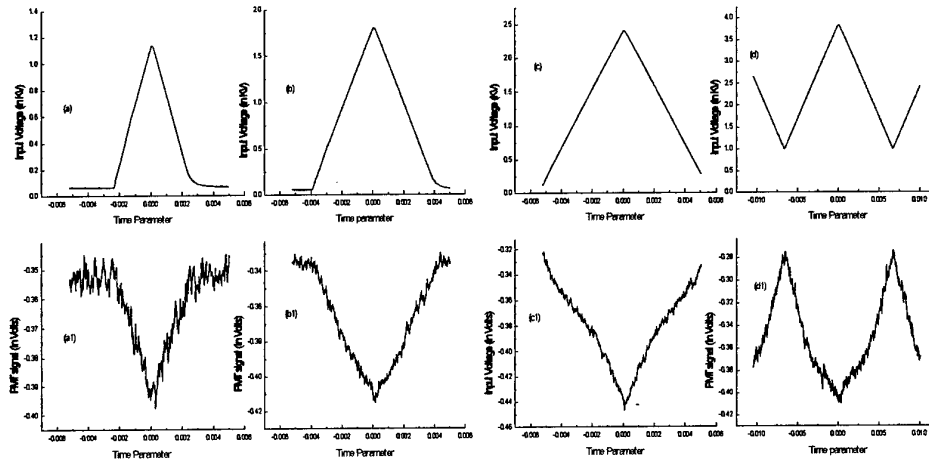


Figure 4.3 The change of fringe intensity with phase-plate (PP) rotation. The thickness of PP is 1.2 mm and the angle of incidence of the beam is  $11.5^\circ$ .

The strain obtained for different voltages are used to calculate the piezoelectric coefficient. As the beam experiences reflection, the actual strain will be half of the optical path change multiplied by the cosine of the angle of incidence at the crystal surface. If the optical path change is measured to be  $p$  and the actual crystal length change is  $\delta l$ , then  $\delta l = (p \cos\theta)/2$ , where  $\theta$  is the angle of incidence of the beam at the crystal surface. Table 4.1 gives a concise set of data for strain with voltages. The average value for the coefficient  $d_{23}$  is  $7.23 \times 10^{-12} \text{ mV}^{-1}$ .



Fi

g. 4.4 PMT signal pulses (lower traces) corresponding to various high voltage pulses (upper traces).

Table 4.1. Calculation of piezoelectric coefficient from the measurement of change of fringe intensity with high voltage pulses across the crystal.

High Voltage / kV	Change in fringe intensity / Volts	Change of optical path length ( $\text{\AA}$ )	Crystal elongation / nm	$d_{23}$ / pm $V^{-1}$
1.07	0.04	184	7.97	5.7
1.75	0.08	368	15.93	7.0
2.28	0.13	598	25.89	8.7
2.82	0.14	644	27.89	7.6

## REFERENCES

1. R. W. Dixon and M. G. Cohen, Appl. Phys. Lett., **8**, 205 - 207, (1966).
2. Acousto-optic Devices and their Applications, L.N. Magdich & V.Y. Molchanov, Gordon and Breach, London, (1989).

## 5. MEASUREMENT OF THE PHOTO ELASTIC COEFFICIENTS OF MBANP

The principal aim of this experiment is to determine the change in refractive index in a material produced by an imposed strain. Strain is developed by generating a travelling ultrasonic wave in the material and the influence of this on the refractive index probed by passing a light beam orthogonal to the ultrasound propagation direction. If the ultrasound wavelength is sufficiently small ( $<100\mu\text{m}$ ) the light will be diffracted by the 'grating' produced by the wave and from a knowledge of the ultrasound and light intensities a component of the photoelastic tensor in the material can be calculated. Dependent on the ultrasound wavelength and the width of the ultrasonic beam the diffraction will be of either Raman-Nath or Bragg type.<sup>2</sup>

### THEORY

The major practical problem is how to quantify the amplitude of the ultrasonic wave. In absolute terms this requires a knowledge of the efficiency of the transducer that converts RF electrical power to ultrasound and the losses associated with the coupling between the transducer and the sample; factors which are difficult to assess precisely. Dixon and Cohen<sup>1</sup> demonstrated a comparative method using a pulsed ultrasonic source which overcomes these problems provided that the transmission losses through any given interface coupling are reciprocal. It is essential that the ultrasonic beam retrace its path exactly upon reflection in order to ensure this. Clearly, this requires that the ultrasonic beam approaches each interface at normal incidence. Figure 5.1 illustrates the ultrasonic pulse sequence, but for clarity the incidence angle is deliberately increased from the zero value actually used in the experiment.

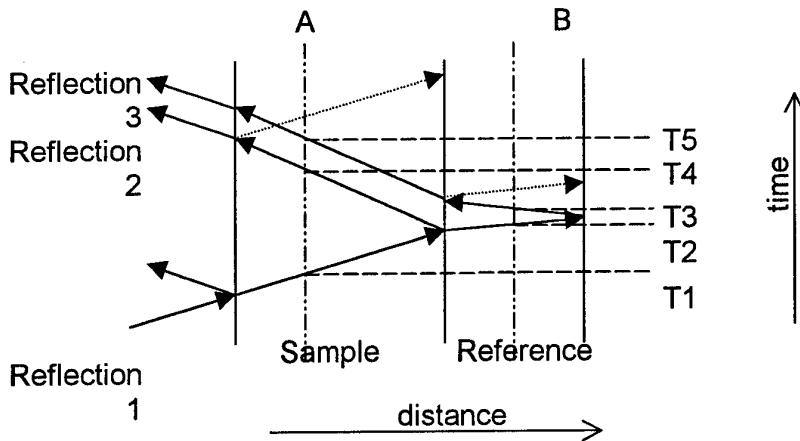


*Fig. 5.1 Annotation of the reflections and pulse timings in the Dixon-Cohen geometry.*

An incident pulse into the sample is partly reflected (reflection 1) and partly transmitted. The transmitted portion is partly reflected at the sample / reference interface producing reflection 2 and partly transmitted into the reference. The reflection from the free surface of the reference meets the interface and is itself partly transmitted producing reflection 3 and partly

reflected. It can be proved that, regardless of the losses at each interface, the product of the acoustic pulse amplitude at times T1 and T5 in the sample is equal to the product of the acoustic pulse amplitude at times T2 and T3 in the reference. Light through the sample at A will be diffracted at times T1, T4 and T5 as the ultrasound passes. Similarly, light directed through the reference will be diffracted at times T2 and T3. From measurements of the intensity of each diffracted beam at times T1, T2, T3 and T5 and the relationship of the acoustic amplitudes the acousto-optic coupling coefficient in the sample can be deduced.

Evidently the experiment requires that the pulses be resolvable in time. For samples of realistic dimensions  $\sim 10$  mm the normal range of ultrasonic velocities in solids ( $10^3$ -  $10^4$   $\text{ms}^{-1}$ ) imposes an upper limit on the pulse width of  $\sim 1\mu\text{s}$  and a upper limit on the light beam of  $\sim 1\text{mm}$ . Since the deflection produced by the grating is  $\sim (\text{light wavelength})/(2*\text{sound wavelength})$ , the divergence of the light beam has to be  $< \sim 500\text{nm}/\sim 200\mu\text{m}$  (i.e.  $< 2.5$  mrad).

### EXPERIMENTAL EQUIPMENT

The light source was a 10mW, plane polarised, Melles Griot He-Ne laser. Its beam width was 0.5 mm FWHM and it had a divergence of  $\sim 0.6$  mrad.

Ultrasound was generated by a Lithium Niobate crystal bonded to a fused quartz buffer rod 70mm long and 15mm diameter. The active electrode on the Lithium Niobate was 5mm diameter and this determined the diameter of the ultrasonic beam. RF power was provided by an HP8640B signal generator connected to an EIN 3202 RF power amplifier. The signal generator was gated by a Lyons PG73N pulse generator.

The optical configuration had the sample mounted on an XYZ stage with an additional axis of rotation about the vertical. The laser to sample distance was  $\sim 100\text{mm}$  and the path length from the sample to the 1mm diameter aperture in front of the EMI 9558B photomultiplier was  $\sim 2$  m. The arrangement is shown schematically in Fig. 5.2.

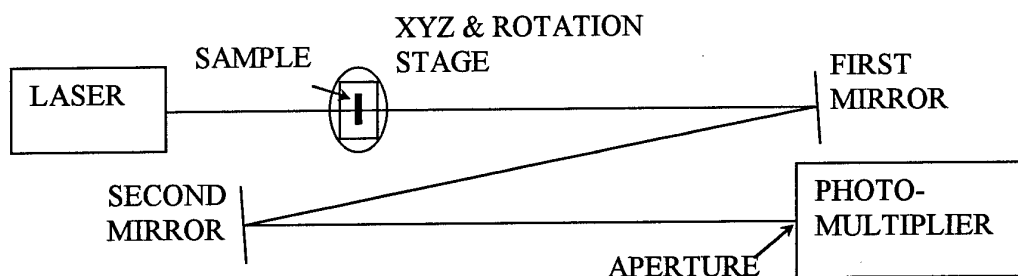


Fig. 5.2 Schematic representation of the optical signal detection geometry

The MBANP crystal was mounted on top of the quartz buffer rod and a further Lithium Niobate reference crystal mounted on top of the MBANP crystal. Paraffin oil was used to facilitate the acoustic couplings at each interface. This order of materials is not the optimum, because the organic crystal is most likely to introduce distortions in the acoustic beam and these would be propagated throughout the entire experiment. Moreover, higher pressure is also required on the sample to ensure adequate coupling between the quartz buffer and organic crystal as well as between the organic crystal and the Lithium Niobate. Such pressure can cause the organic crystal to cleave in certain orientations. However, this configuration is forced upon us at this time by the need to prevent the repeat set of acoustic

pulses (6 onwards) from overlapping the pulse signal from reflection 5 (fig. 1). This is determined by the acoustic velocities and the dimensions of the Lithium Niobate available in our laboratory.

Fig. 5.3 shows a partially disassembled configuration with the laser beam passing through the Lithium Niobate

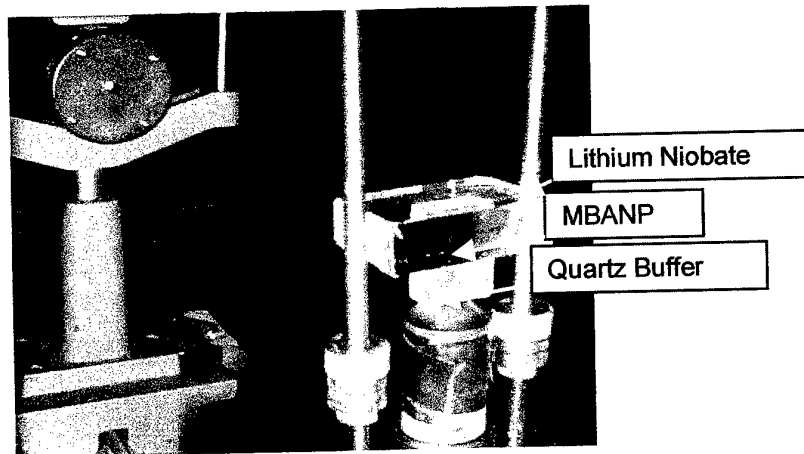


Fig. 5.3 Photograph of the experimental arrangement, showing the laser propagating through the Lithium Niobate reference crystal.

An exploded view of the quartz rod, MBANP and Lithium Niobate is shown in Fig. 5.4. The laser light was directed along the [001] direction of the MBANP or the Y direction of the Lithium Niobate as required. The 5mm diameter ultrasonic beam passed along the quartz buffer rod, through the MBANP and the Lithium Niobate with partial reflections at each interface.

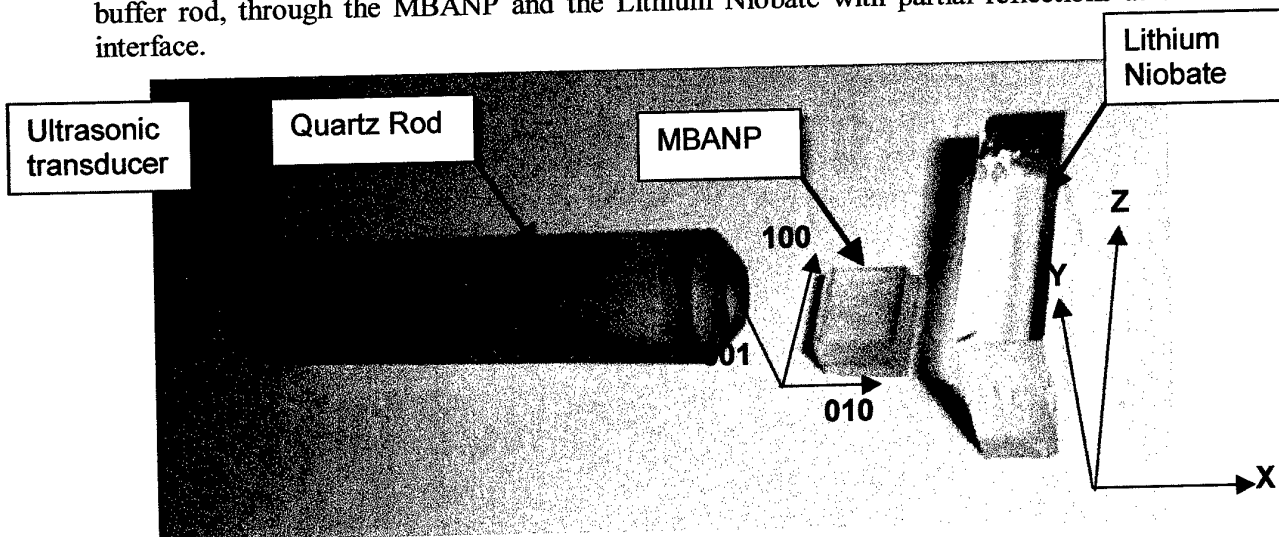


Fig. 5.4 Exploded view of the ultrasonic propagation path, with crystal lattice orientations.

## EXPERIMENTAL PROCEDURE AND RESULTS

The position of the quartz rod / MBANP / Lithium Niobate assembly was adjusted so that the light beam passed through the Lithium Niobate and interacted with the ultrasonic pulse. The ultrasonic signal generator was operated at 36 MHz and the pulses were  $0.5\mu\text{s}$  long with a repetition rate of a few kHz. The photomultiplier was located so that the first order diffracted beam, for the light polarised along the Z axis of the Lithium Niobate and propagating in this reference crystal, fell on its aperture and the photomultiplier output was recorded using a Tektronix DSA 602A digital signal analyser. The output, was as shown in Fig. 5.5.

The time separation of the pulses 2 and 3 (Fig. 5.1) is that caused by the ultrasonic pulse in travelling to the free surface of the Lithium Niobate and back. The assembly was then reconfigured so that the light was positioned within the ultrasonic beam in the MBANP crystal and the output (from the first diffraction peak) was as shown in Fig. 5.6.

The time separation of the pulses 1 and 4 (Fig. 5.1) is that caused by the pulse in travelling to the MBANP/Lithium Niobate interface and back. The time separation of the pulses 1 and 5 (Fig. 5.1) is that caused by the pulse in travelling to the free surface of the Lithium Niobate and back.

The experimental parameters are listed in Table 5.1.

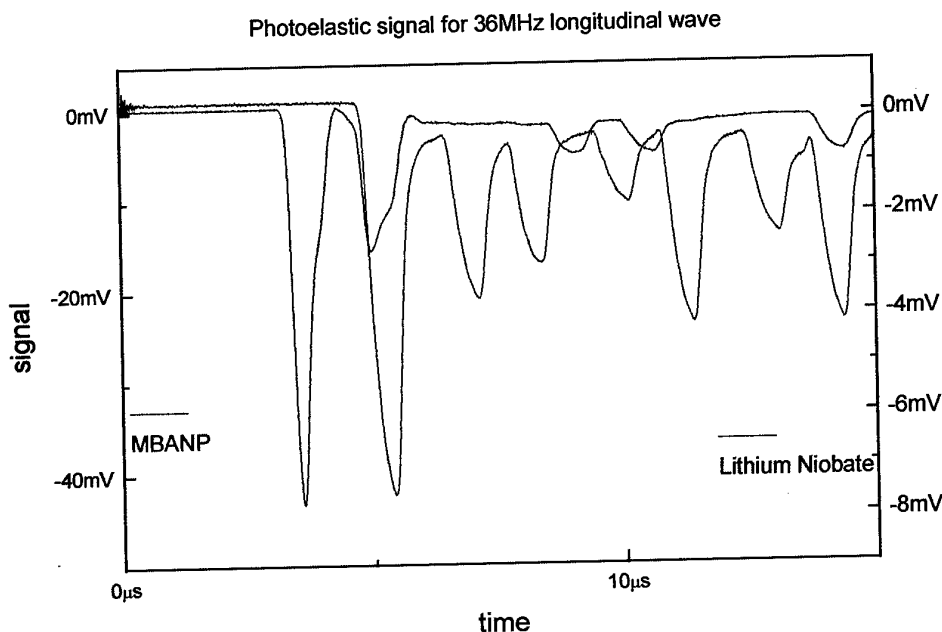


Fig. 5.5 The optical signal generated from the MBANP organic crystal.

Table 5.1 Parameters Relating to the Dixon-Cohen Experiment

Material	Ultrasonic Wave Direction	Light Wave Direction	Light Polarisation Direction	Refractive Index	Acousto-optic Coefficient	Specific Gravity	Ultrasonic Velocity / m.s <sup>-1</sup>
Lithium Niobate	X axis	Y axis	Z axis	2.29 (n <sub>Z</sub> )	0.153 (p <sub>31</sub> )	4.64	7016
MBANP	[010]	[001]	[100]	1.67 (n <sub>X</sub> )	p <sub>12</sub>	1.32	2718

A value for the photoelastic coefficient, p<sub>12</sub> for the MBANP can be calculated from the relationship of Dixon and Cohen<sup>1</sup>;

$$\left( \frac{I_1^{\text{MBANP}} \cdot I_5^{\text{MBANP}}}{I_2^{\text{LiNbO}_3} \cdot I_3^{\text{LiNbO}_3}} \right)^{\frac{1}{2}} = \frac{\left( \frac{p^2 \cdot n^6}{\rho \cdot v^3} \right)^{\text{MBANP}}}{\left( \frac{p^2 \cdot n^6}{\rho \cdot v^3} \right)^{\text{LiNbO}_3}}$$

Where n is the refractive index, p is the photoelastic coefficient, ρ is the density and v is the speed of ultrasound. However, this value will not be truly representative of the material. Not only was the orientation of the MBANP chosen because the cleavage faces gave a minimal scattering of the laser beam and the best coefficient is probably not being exploited, but there are deviations of the present experiment from the Dixon-Cohen model.

It is unlikely that the intensity of the second ultrasonic pulse is much less than the third pulse in the Lithium Niobate. That this should appear so in Fig. 5.5, is undoubtedly an artefact and not due to acoustic absorption. In the original Dixon Cohen paper these pulses had amplitudes within a few percent of each other. A likely explanation of the observations of Fig. 5.5 is that the outgoing pulse has not approached the free surface normally and so has not reflected normally. The laser would then not be sampling the same region of the acoustic pulse wavefront in both cases. A similar state of affairs would also occur in the MBANP. In most circumstances such a misalignment of the acoustic beam would give rise to an underestimate of the coefficient of the MBANP. This misalignment may be owing to inadequately polished coupling faces in the MBANP crystal. This would result in the launching of a distorted ultrasonic wave into the MBANP crystal and this problem would propagate throughout the experiment.

The 36MHz ultrasonic frequency was chosen because this gave a reasonable combination of ultrasonic pulse intensity and diffraction angle. Raman-Nath diffraction was the dominant mechanism in both the MBANP and the Lithium Niobate. Raman-Nath diffraction has the disadvantage of being less efficient than Bragg diffraction but the advantage of being less sensitive to the precise angle between the light and ultrasound wavevectors. The experiment should be performed in the Bragg regime, but 36 MHz is the highest useful frequency available to us with our present equipment. This is a very important limitation on the present experiment.

The photomultiplier pulses were distinctly asymmetric with a significant tail although the acoustic pulses themselves were reasonably symmetric. The source of this problem requires

further investigation, but it does mean that the gaussian fits used to estimate the pulse amplitudes are rather approximate.

There was significant loss of intensity in the optical signal from the MBANP crystal. This was attributed to either scattering at the crystal surface or from defects within the crystal. Since the MBANP crystal sample was known, from synchrotron X-ray topography to contain remarkably few defects, these would have to have arisen from excessive pressure applied in this experiment to ensure efficiency at the multiple coupling interfaces. That this intensity loss was not caused by ultrasonic absorption was shown by measuring the propagation (longitudinal) velocities of the ultrasound in both Lithium Niobate and MBANP. Velocity measurements were carried out by a conventional pulse echo overlap method over a range of frequencies and the results are shown in fig. 5.6.

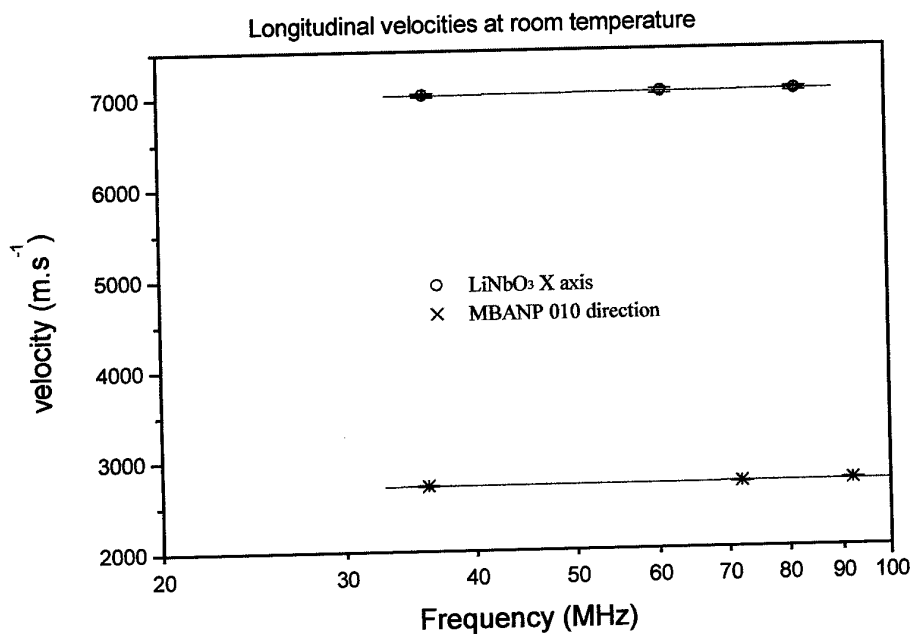


Fig. 5.6 Longitudinal velocities as a function of ultrasonic frequency (dispersion curves) for Lithium Niobate and MBANP.

The error bars represent the standard deviation from the plots and are an indication of the reproducibility of the results for the particular samples. By analogy with the Kramers-Kronig relationship, the variation of velocity with frequency gives an estimate of the attenuation due to absorption mechanisms. Since the slope of velocity vs.  $\log(\text{frequency})$  is similar in the MBANP ( $30\text{m.s}^{-1}.\text{decade}^{-1}$ ) and the Lithium Niobate ( $45\text{m.s}^{-1}.\text{decade}^{-1}$ ) it can be inferred that the absorption in MBANP is similar to that in Lithium Niobate, i.e. not significant in the context of these experiments.

Notwithstanding the limitations discussed above, arising from our having to use available equipment, the value of the photoelastic coefficient for MBANP in the single orientation described above is 0.035 at 36 MHz. This compares with 0.153 for the lithium niobate. Although this value is disappointingly low, it must be remembered that the MBANP

orientation was almost certainly not optimised and the experiment was not the originally proposed Bragg diffraction.

## 6. SUMMARY AND FUTURE WORK

Materials in acousto-optics are frequently assessed according to the figure of merit:

$$M = n^6 p^2 / \rho v^3$$

There are two components to the photoelastic coefficient,  $p$ . The first depends on the density changes and consequently on the elastic constants of the material when stressed. This is the primary photoelastic effect. The second arises when a crystal lacking a centre of symmetry is stressed. In this case the accompanying piezoelectric effect produces an electric field which induces the electrooptic effect giving rise to the second component, i.e. the secondary photoelastic effect. Since MBANP is strongly electrooptical and piezoelectric, the secondary photoelastic effect is expected to be significant. MBANP has a low acoustic velocity (2718 m s<sup>-1</sup>) and a low density (1.32 g cm<sup>-3</sup>), both of which favour a high figure of merit. The refractive index (1.67) is not quite as large as that of the lithium niobate (2.29) at 632.8 nm, although this can be much higher, being strongly wavelength and orientation dependent. Therefore a large figure of merit is expected for MBANP. Of course, all the properties except the density are tensorial and the optimal configuration for the highest  $M$  should be found.

Thus, although the photoelastic coefficient of MBANP is lower than that of lithium niobate, the figure of merit,  $M$ , is  $1 \times 10^{-18} \text{ s}^3 \text{ g}^{-1}$ . This compares well with  $2.1 \times 10^{-18} \text{ s}^3 \text{ g}^{-1}$  for LiNbO<sub>3</sub>. However, for high performance materials,  $M$  values are typically<sup>1,2</sup>  $3 \times 10^{-17} \text{ s}^3 \text{ g}^{-1}$  for PbMoO<sub>4</sub> and  $8 \times 10^{-16} \text{ s}^3 \text{ g}^{-1}$  TeO<sub>2</sub>. From Fig. 5.5, it is clear that the light intensity diffracted by the MBANP is over 5 times that from the lithium niobate, so that, even in this very non-optimised experiment, MBANP is out-performing the inorganic material in efficiency.

The work on this single orientation of one organic material has been progressed as far as possible with the equipment and time available. Clearly, the optimum orientation for the optoacoustic effect of MBANP should be determined, since it is known that in this orientation the piezoelectric effect, measured as  $d_{23}$  above, is at its minimum, thus minimising the electrooptic component and the secondary photoelastic effect. The true efficiency of MBANP is not being shown in the present Raman Nath configuration, but in order to access the Bragg regime, much higher ultrasonic frequencies would have to be used (150 – 200 MHz) necessitating generators and driving transducers which are not presently available to us. Other analogous materials have not been examined, although they have higher refractive indices. Therefore higher figures of merit would be expected. The optical wavelength of 632.8 nm is not the most relevant for many applications. Green light around 500 nm would raise the refractive indices of these materials, yet further improving their performance. These materials show definite promise, but this could not be explored in the present, limited, pilot study.

## REFERENCES

- 1.) D.A. Pinnow, IEEE J. Quant. Electr. QE-6, 223 (1970).
- 2.) N. Uchida and Y. Ohmachi, J. Appl. Phys. 40, 4692 (1969).